Role of oxidation in thermal fatigue damage mechanisms and life of X38CrMoV5 (AISI H11) hot work tool steel

M. Salem, Sabine Le Roux, Gilles Dour, A. Vande Put

International Journal of Fatigue 190 (2025) 108584

Contents lists available at ScienceDirect

International Journal of Fatigue

journal homepage: www.elsevier.com/locate/ijfatigue

Role of oxidation in thermal fatigue damage mechanisms and life of X38CrMoV5 (AISI *H*11) hot work tool steel

M. Salem [a,*], S. Le Roux [a], G. Dour [b], A. Vande Put [c]

[a] Institut Clément Ader (ICA), Université de Toulouse, CNRS, IMT Mines Albi, UPS, INSA, ISAE-SUPAERO, Campus Jarlard, 81013 Albi, France
[b] Advisian, Worley Parsons, Perth WA 6000, Australia
[c] CIRIMAT, Toulouse INP, Université Toulouse 3 Paul Sabatier, CNRS, Université de Toulouse, 4 allée Emile Monso, BP 44362, 31030 Toulouse cedex 4, France

ARTICLE INFO

Keywords:
Tool steel
Thermal fatigue
Oxidation
Crack initiation
Heat-checking

ABSTRACT

Hot work tools steels, which are submitted to severe solicitations in service, are often damaged by thermal fatigue and corrosion. Interrupted Thermal Fatigue experiments were performed on X38CrMoV5 tool steel between 100 and 650 °C, in air and reduced oxygen partial pressure atmospheres after primary or secondary vacuum. A thermal and thermo-mechanical analysis by finite element method was carried out to estimate the strains and stresses undergone by the axisymmetric disc-shaped specimen during thermal cycling. The morphology, structure and phase composition of the oxide layer were analysed using scanning electron microscopy, energy dispersive spectroscopy and X-ray diffraction. It was shown that the thickness, homogeneity, structure, and compacity of the oxide multilayer formed on the specimen changed depending on test atmosphere. In air, crack initiation and propagation were strongly assisted by oxidation, leading to reduced fatigue life compared to inert atmospheres. Steel softening was highlighted in sub-surface, whatever the test atmosphere.

1. Introduction

Steels for hot work tools such as AISI H11 and H13 martensitic grades are commonly used, due to their thermo-physical and thermo-mechanical properties at high temperature, in particular their excellent combination of toughness and hardness [1–4]. In high temperature forming processes as for example die casting, forging, rolling, hot extrusion or hot stamping, the tools subjected to thermal heating and cooling cycles experience large transient temperature variations. The thermal expansion and contraction of the material generate cyclic stresses and mechanical deformation [4–10]. Consequently, the tools are severely damaged by thermal fatigue, which is manifested by the formation of a network of fine surface cracks often called “heat checking” [2,4,7,8,11–18]. In addition, cyclic thermo-mechanical solicitations are often coupled with corrosive atmospheres, exposing the tool to oxidation or corrosion reactions which reduces the lifespan of tools and dies [8,9,19–21].

Among the factors leading to initiation and propagation of thermal micro-cracks, the atmosphere is known to play a significant role [4]. Several studies have indeed shown that initial crack growth was promoted by the oxidation of surface cracks [22–25]. A reduction in the lifespan of steel through oxidation is often observed, even in the presence of protective coatings against wear, corrosion or thermal fatigue [26–31]. The environment also has an effect in depth, with a change in the chemical composition of the steel sub-surface [32,33] and possible formation of oxides or intermetallics inside the cracks [16,32–34]. Ebner et al., by heating a flat specimen by laser under an inert atmosphere, succeeded in producing a thermal fatigue test without oxidation, thus highlighting damage by plastic deformation under biaxial loading [8]. However, there is still a lack of knowledge about the influence of oxidation on the initiation and propagation of thermal fatigue cracks, as stated by da Silva et al. from a detailed literature review on thermal fatigue of hot work tool steels [3]. In particular, the mechanisms resulting from the complex interaction between thermal fatigue and oxidation have not been clearly demonstrated.

On a laboratory scale, thermal fatigue tests are performed by abruptly heating and cooling the specimen surface cyclically. This complies the definition of Spera, who defined thermal fatigue as a gradual deterioration and eventual cracking of a material by alternate heating and cooling during which free thermal expansion is partially or completely constrained [35]. Different test setups can be used, varying by the heating and cooling method (laser pulse, electromagnetic induction, immersion into liquids, fluidizing beds heating, flame heating, etc.) and the specimen geometry (simplified structures such as cylinder

* Corresponding author.
E-mail address: mehdi.salem@mines-albi.fr (M. Salem).

https://doi.org/10.1016/j.ijfatigue.2024.108584
Received 19 July 2024; Received in revised form 21 August 2024; Accepted 1 September 2024
Available online 2 September 2024

or cube [11,14–16,19,2,3,31,36–48,6]). The selected damage criterion can also change depending on the authors [16,33,41,49]. The lack of standardization of this specific fatigue test, already noted by Howes in his time [33], makes it difficult – if not impossible – to compare results when test conditions and sample geometries differ [3,50]. However, a simulation analysis can allow a relative comparison of fatigue resistance, using mechanical criteria derived from numerical calculations [3,8].

In the absence of a reference test decoupling the damage mechanisms induced by thermal fatigue and oxidation, this study aims to better understand the effect of environment, especially the partial pressure of oxygen, on the damage of a X38CrMoV5 (AISI H11) steel. The proposed experimental approach consists of first carrying thermal fatigue tests between 100 and 650 °C under argon and nitrogen (reduced PO_2), in order to determine damage and life specific to thermal fatigue loading. Tests carried out under the same conditions, but in an oxidizing atmosphere (air), will then highlight the role of oxidation in the damage mechanisms. Based on detailed microstructural observations and analyses, combined to a thermo-mechanical analysis by finite element method (FEM), the mechanisms of both oxidation and crack initiation and propagation will be assessed and discussed.

2. Experimental procedure

A low silicon and impurity grade of X38CrMoV5 tool steel (AISI H11), known as ADC3, was investigated. This alloy contains 0.36 % C, 5 % Cr, 1 % Mo, and 0.35 % Si in addition to Fe (in weight %). A heat treatment (by austenitisation at 980 °C for 1 h, quenching and double tempering at 550 and 605 °C for 2 h) was performed to achieve a martensitic microstructure with a final hardness of about 47 HRC (485 Hv). Disk-shaped axisymmetric specimens, with an axial hole for internal water-cooling and a polished surface in the useful part along θθ direction (tip), were used for thermal fatigue (TF) tests (Fig. 1).

TF experiments were performed using a test bench with a sealed chamber, following a procedure fully described in [51]. Thermal cycles between a minimal temperature (T_{min}) of 100 °C and a maximal temperature (T_{max}) of 650 °C were applied on the top surface of the disk

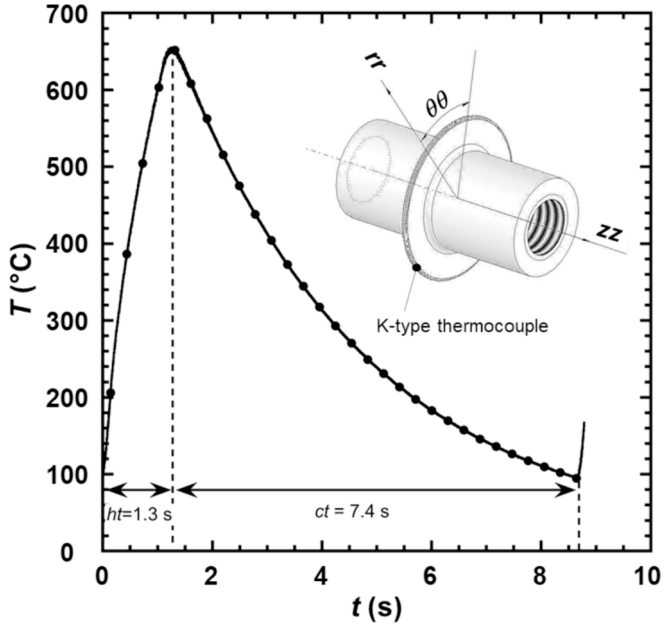

Fig. 1. Thermal cycle (T_{min} = 100 °C, T_{max} = 650 °C) applied on the top of the disk-shaped axisymmetric specimen during the TF test (measured using a thermocouple at the top surface of the specimen, as indicated). The longitudinal (*zz*), circumferential (*θθ*) and radial (*rr*) axes are indicated on the specimen scheme [*ht*: heating time, *ct*: cooling time].

(Fig. 1). The heating time (*ht*) was set to 1.25 s and allowed applying a heat-flux density of 3.22 $MW.m^{-2}$ with a mean heating rate of 420 °C.s^{-1}. The cooling time (*ct*) was fixed such that temperature was cooled down from 650 to 100 °C, with a mean cooling rate of 74 °C.s^{-1}. Before starting the TF tests under inert atmosphere, the reduction of the partial pressure of oxygen in the chamber was ensured by carrying out successive atmosphere purification operations, including a primary or secondary vacuum step followed by an inert gas sweep. Argon and nitrogen, distinguished by their ionization current (breakdown voltage), were used under the conditions of primary ($4x10^{-2}$ mbar) and secondary vacuum ($5x10^{-5}$ mbar), respectively. The corresponding oxygen partial pressure (PO_2) is $8.4x10^{-3}$ mbar and $1.05x10^{-5}$ mbar for the argon and nitrogen atmospheres, respectively. The impurity contents of the gases used are specified in Table 1. The tests were carried out at slight over-pressure (around 1.2 mbar). A total of four TF tests were performed, one under argon, one under nitrogen and two in air.

The TF experiments were regularly interrupted, for example every 500 cycles until 2,500 cycles, then every 2,500 until 20,000 cycles, and then every 5,000 cycles until 30,000 cycles in air. After each interruption, to examine and follow the evolution of the damage, the specimen disk was examined and followed by optical microscopy and scanning electron microscopy (SEM). In addition to these microstructural observations, energy dispersive spectroscopy (EDS) analyses and EDX mapping were carried out in order to determine the chemical elements composing the oxide layer. The oxide phases were identified by X-ray diffraction (XRD), using a Panalytical X'Pert Pro diffractometer with monochromatic CuK_α radiation (λ = 1.54 Å) and point detector. XRD analysis were performed in conventional *2θ* acquisition mode, using the following parameters: angular step size = 0.01°, integration time = 15 s, voltage = 40 kV, and current = 40 mA. The macro-cracks initiating and propagating on the disk were measured by direct observations, in order to determine crack propagation curves (evolution of the crack length *a* as a function of the number of cycles *N*).

After the final number of TF cycles was achieved, the specimen was cut and polished cross-sections were prepared for detailed SEM investigations of in-depth damage and microstructural evolutions. In addition, a series of 13 Vickers micro-hardness indents were made from the surface to 3.5 mm in depth (following *rr* axis), with increasing inter-indent distance. A load of 200 g ($Hv_{0.2}$) was applied for 10 s. The first indent was positioned in the steel, just below the interface with the oxide layer.

3. Thermal and thermo-mechanical analysis

During the TF test, the heat flux density applied to the surface of the specimen, combined with continuous internal cooling, created thermal transients inside the disk. The propagation of the thermal wave towards the coldest areas induced thermal cycles of different amplitudes and kinetics. The expansion mismatch between the hot and the colder underlying zones generated a mechanical strain varying depending on time, temperature and position in the specimen. This self-constraint induced a thermo-mechanical cycle responsible for the TF process [17].

To estimate the evolution of temperature, strain and stress in the specimen as a function of time, numerical simulations were carried out using the Finite Element Method (FEM), based on previous works [52,53]. Uncoupled thermal and thermo-mechanical analyses were conducted using ABAQUS®.

The material behaviour is assumed to be thermo-elasto-plastic (TEP) with isotropic hardening. It should be noted that, for the modelling of

Table 1
Impurity content of argon and nitrogen gases used for the TF test environments.

	H_2O	O_2	C_nH_n
Argon (αAr)	< 3 ppm	< 2 ppm	< 0.5 ppm
Nitrogen (αN_2)	< 3 ppm	< 2 ppm	< 0.5 ppm

the steel life – which is not the subject of this study –, a thermo-mechanical simulation using a thermo-elasto-visco-plastic behaviour taking into account the kinematic and isotropic hardening that describes the cyclic hardening or softening and the Bauschinger effects, would be more relevant. The TPE model parameters were determined from isothermal tensile tests performed in a temperature range from 20 °C to 650 °C and at a stress rate $\dot{\sigma} = 6$ MPa.s^{-1} (which corresponds to a strain rate of $\dot{\varepsilon} = 3$ to 4.10^{-5} s^{-1}). The hardening curves were identified for the plastic part of the tensile curves (σ-ε_{in}) by linear regression in a logarithmic coordinate system. Thus, the TEP model at different temperatures was defined by a Ramberg-Osgood type law, described by the following equations:

$$\varepsilon_{tot}(\sigma, T) = \frac{\sigma}{E(T)} + \left(\frac{\sigma}{K(T)}\right)^{M(T)} \quad (1)$$

$$\varepsilon_{tot}(T) = \varepsilon_{el}(T) + \varepsilon_{in}(T) \quad (2)$$

and

$$\varepsilon_{el}(T) = \frac{\sigma}{E(T)} \quad (3)$$

where ε_{tot}, ε_{el} and ε_{in} are respectively the total, elastic and inelastic strains, σ is the stress, E is the Young modulus, K and M are the material parameters depending on the temperature T. The obtained hardening law parameters (given as a function of the temperature in Table 2) were implemented in ABAQUS® as discrete numerical data pairs for each temperature. The Young modulus (E) and the yield stress ($\sigma_{0.2}$ with 0.2 % strain offset) as a function of temperature, are also presented in Table 2.

Due to geometric symmetry, only a quarter of the specimen was modelled. The specimen was meshed with axisymmetric solid elements for thermal (DCAX8, eight-node quadratic) and mechanical (CAX8, eight-node bi-quadratic) analysis, respectively. Near the edge of the specimen, the mesh was refined with elements of approximately 15 μm (Fig. 2a). It should be emphasized that the oxide layer which may form on the specimen was not considered in this numerical simulation.

The thermal simulation was carried out based on heat flux and temperature measurements, using a specimen instrumented by several K thermocouples spot welded on the disk at different depths (Fig. 2a). Heat flux densities over time were imposed on the external surface (at the disk tip), considering convective and radiative heat transfers. For the internal surface, a constant heat transfer coefficient, calculated by an analytic model, was used. The relevance of the boundary conditions used for the estimation of transient thermal loadings was attested by the good match between the measured and calculated temperature–time cycles (Fig. 2b). For the thermo-mechanical calculations, tensile curves were measured from room temperature to 650 °C. The thermo-physical properties (thermal expansion, specific heat, density) of the steel were also measured in the same temperature range. The simulation was compiled for five consecutive cycles.

Fig. 3a and b respectively represent the mechanical stresses as a function of time, and the mechanical hysteresis-strain loops, calculated for an element of the upper surface of the disk during the first five TF cycles. They revealed that under TF cycling conditions, the specimen underwent alternating compression/tension under uniaxial thermo-mechanical cyclic loading along the circumferential $\theta\theta$ axis.

During the first heating–cooling cycle, an evolution of the mechanical loading (stresses and deformations) can be observed and broken down as follows:

- zero stress and strain at 20 °C (point A);
- low amplitude compression during the preheating period, up to 100 °C (AB);
- strong evolution during the heating period from 100 to 650 °C (BD), with a compression peak ($\sigma_{\theta\theta} = -755$ MPa) observed at 500 °C (point C) and an ever-increasing plastic deformation, associated with a decrease in stress from 500 to 650 °C (CD);
- release of compressive loads during cooling from 650 to 100 °C (DE), with a passage in tensile stresses reaching its maximum ($\sigma_{\theta\theta} = 550$ MPa) at 100 °C (point E).

It can be seen that the loading undergone by the specimen during the first heating remained thermo-elastic up to 400 °C ($\sigma_{\theta\theta} = 720$ MPa), with plastic deformations appearing beyond this temperature (because the yield strength of the steel was reached at these levels of temperature and stress). This reflects a drop in the mechanical properties of the steel beyond 500 °C (at the end of the first TF cycle).

From the second cycle, an evolution of the cyclic loadings according to a quasi-thermo-elastic asymptotic path was highlighted, with a low plastic deformation (D-E-D on Fig. 3b). A stabilization of the thermo-mechanical cycles can be observed from the second cycle, due to the choice of the thermo-mechanical behaviour law in the simulation (as shown in Fig. 3a with a repeated applied stress path D-E-D-E-D-E … for the subsequent cycles). In stabilized regime, the maximum tensile stress was achieved at the minimum temperature (T_{min}) of the TF cycle, while the maximum compressive stress was achieved at the maximum temperature T_{max}.

4. Effect of environment on TF damage

4.1. Air

In ambient air, a uniform, homogeneous and multi-layered oxide was formed on the surface of the specimen in the early hundred thermal cycles. This oxide was composed of an upper layer of hematite (Fe_2O_3), covering a layer of magnetite (Fe_3O_4) with a columnar structure. A spinel magnetite phase, rich in chromium ($(Fe,Cr)_3O_4$), was revealed at the oxide/steel interface (Fig. 4a). The total thickness of the oxide scale layer was estimated at about 25 μm after 30,000 TF cycles. The thickness of the hematite layer was estimated at less than 20 % of the total oxide thickness, while the magnetite and spinel layers had quasi-identical thicknesses (as also observed under isothermal aging tests [54]). The upper hematite layer appeared to be more porous than the inner layer of spinel, which was quite compact and adherent to the substrate. Its surface morphology seemed also to evolve during the thermal cycling, from an alveolar structure at low number of cycles to a mixed alveolar-spangled structure at higher number of cycles (Fig. 4b) [55].

As shown in Fig. 5a, some micro-cracks initiated locally in the oxide layer after only few hundred TF cycles. From 1,500 to 2,500 cycles, a network of regularly spaced micro-cracks ("heat-checking") covered the whole surface (Fig. 5b). This indicates that the micro-cracks first propagated through the oxide multilayer, along rr and zz directions (i.e. perpendicularly to the orthoradial $\theta\theta$ loading). From 5,000 cycles, some micro-cracks presenting opened lips at room temperature, propagated

Table 2
Thermo-mechanical properties of X38CrMoV5 and parameters of the Ramberg-Osgood law at different temperatures.

T (°C)	20	200	300	400	500	550	600	650
E (GPa)	213	206	193	185	168	151	143	121
$\sigma_{0.2}$ (MPa)	1206	1112	1065	1017	880	758	605	430
K (MPa)	2008	1884	1875	1940	1904	1935	1949	1846
M	12.78	11.92	11.21	9.488	7.980	6.680	5.310	4.255

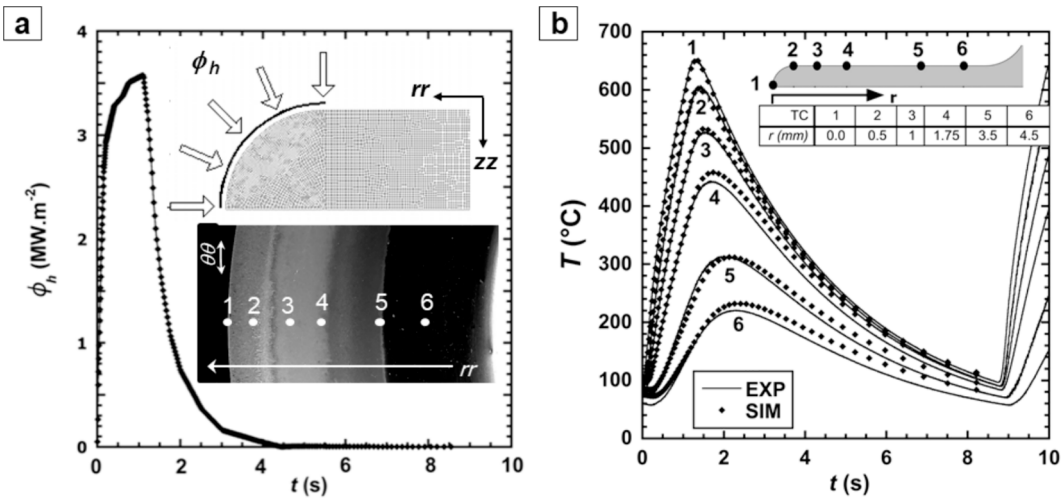

Fig. 2. a) Heat-flux density imposed at the surface of the specimen, ϕ_h versus time t (the inserted SEM image shows the positions of the thermocouples along rr axis and the isothermal concentric rings observed on the specimen after a TF test); **b)** Temperatures measured and calculated (by numerical simulation) at the steel surface, at various distances from the specimen tip along rr (the distances from the tip of the 6 thermocouples are indicated in the table).

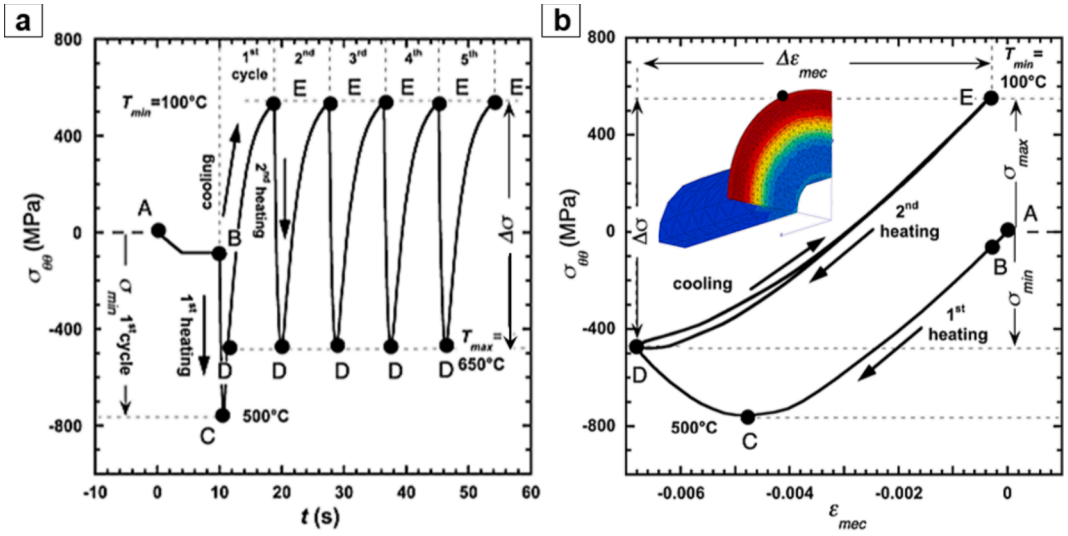

Fig. 3. a) Evolution of the mechanical stresses $\sigma_{\theta\theta}$ vs. time at the top of the disk specimen; **b)** Mechanical hysteresis loops ($\sigma_{\theta\theta}$ vs. mechanical strain ε_{mec}) calculated for the 5 first thermal cycles.

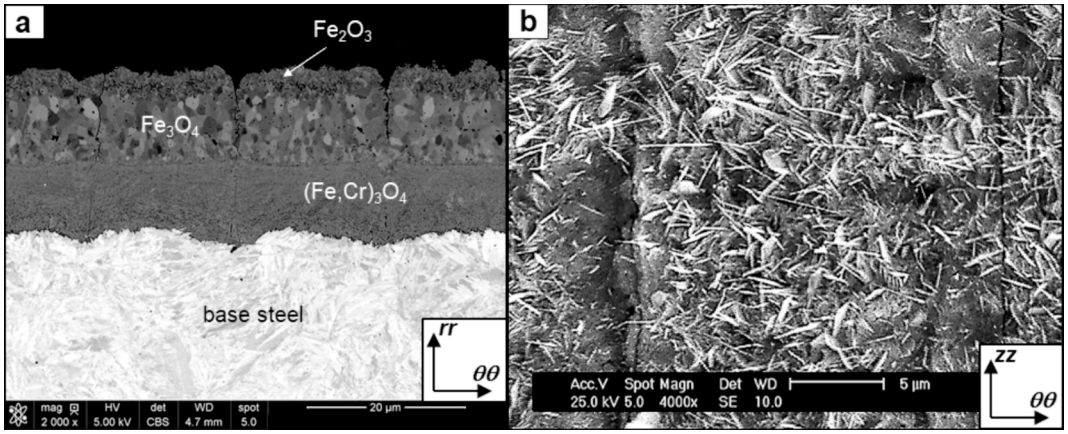

Fig. 4. SEM observation of the oxide scale formed in air after 30,000 TF cycles: **a)** multi-layered structure in cross-section; **b)** mixed alveolar-spangled morphology of the surface hematite layer.

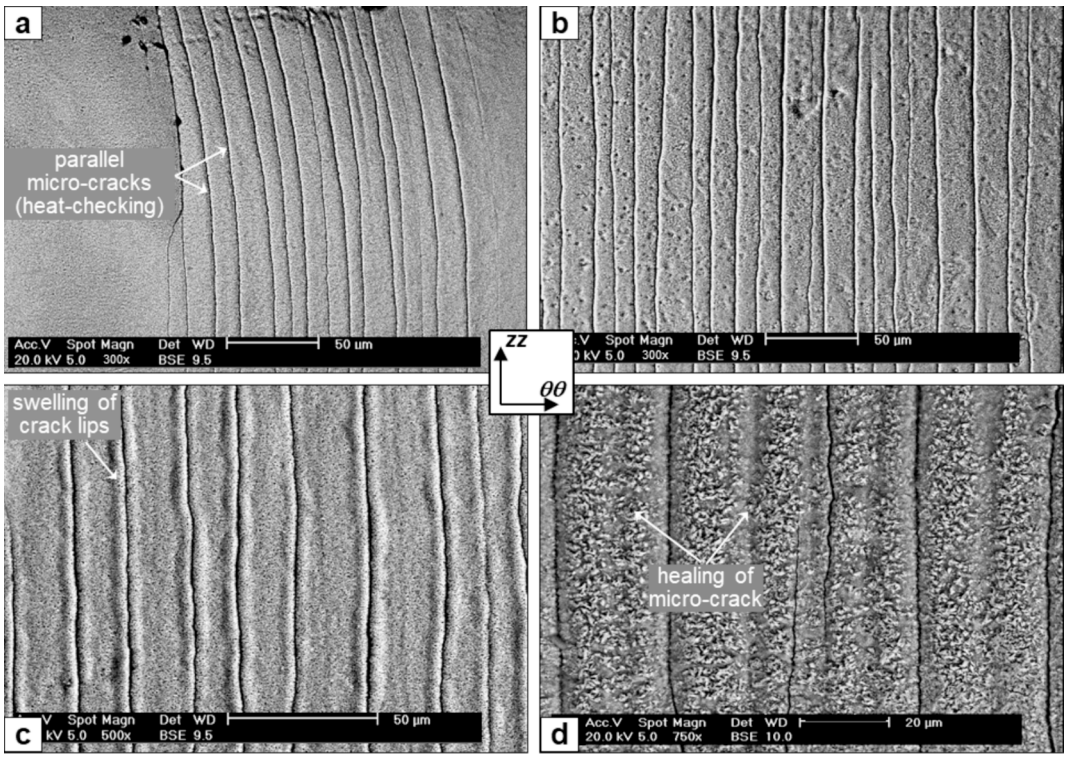

Fig. 5. Evolution of the uniaxial micro-cracking of the surface oxide layer in air, after increasing numbers of TF cycles: **a)** 500, **b)** 2,500, **c)** 5,000 and **d)** 20,000 cycles.

into the steel substrate to form "V-type" short-cracks (Fig. 6a). This resulted in a slight swelling of the lips of micro-cracks in surface (Fig. 5c and Fig. 6a). At higher number of cycles, some so called "secondary" micro-cracks "disappeared" as they were filled by oxide, while some others become more and more open (Fig. 5d). Post-mortem SEM observations in cross-section revealed that at high number of cycles, some micro-cracks propagated in-depth perpendicular to the loading axis, following a very straight path (Fig. 6b). Those cracks were filled with the same multi-layered oxide as observed in surface. In addition, the tip of the crack appeared blunt, likely due to oxidation reactions.

4.2. Argon

A localized and multi-layered oxide again composed of hematite, magnetite and spinel was formed (Fig. 7a), but with a lower thickness than in air (about 15 µm after 30,000 TF cycles, on continuous oxide areas). Detailed SEM observations showed that the morphology of the superficial hematite layer was predominantly alveolar (Fig. 7b).

Heterogeneous oxidation was revealed (Fig. 8), probably due to the lowering of the partial pressure of oxygen in the test atmosphere. At the beginning of the TF cycles, isolated oxide sites ("island-type") were nucleated along the polishing grooves of the specimen surface and aligned along the $\theta\theta$ axis. This kind of localised oxidation along the machining marks has already been reported by Barbehön et al. [56]. On

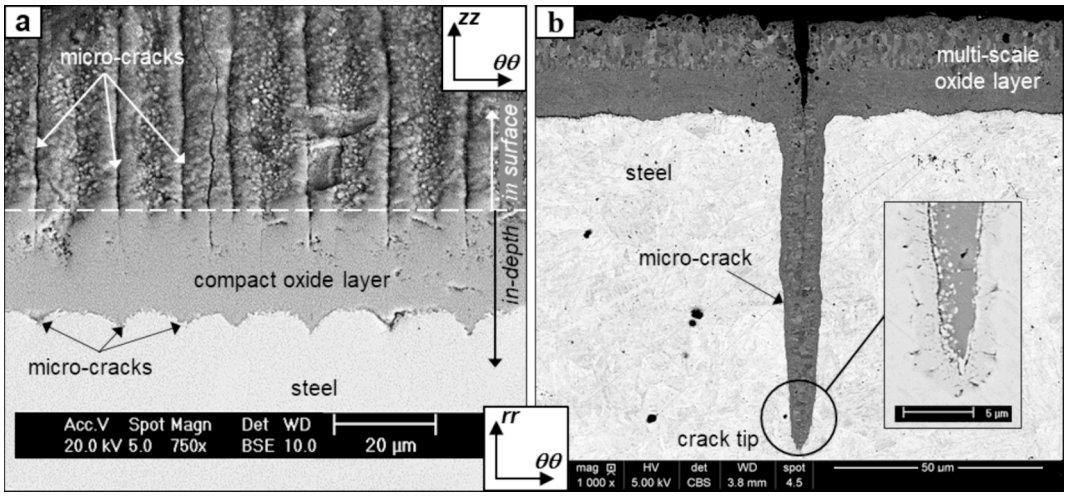

Fig. 6. Post-mortem SEM observations (after 30,000 TF cycles in air): **a)** heat-checking network in the oxide layer (in surface) and corresponding preferential oxide growth in the steel (in-depth); **(b)** propagation of a micro-crack (note the crack entirely filled with multilayer oxidation, and the blunting at the crack tip).

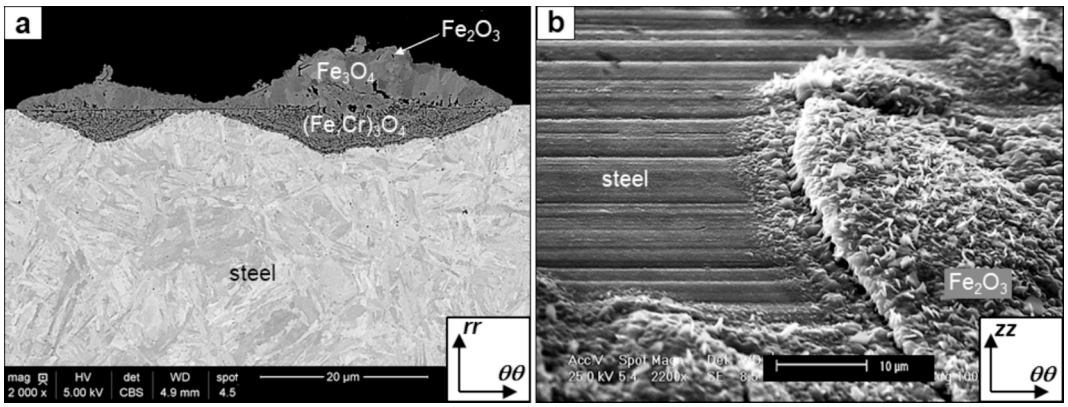

Fig. 7. Morphology of the localized multilayer oxide formed in argon after 30,000 TF cycles: porous laminated structure in cross-section **(a)** and alveolar hematite observed in surface **(b)**.

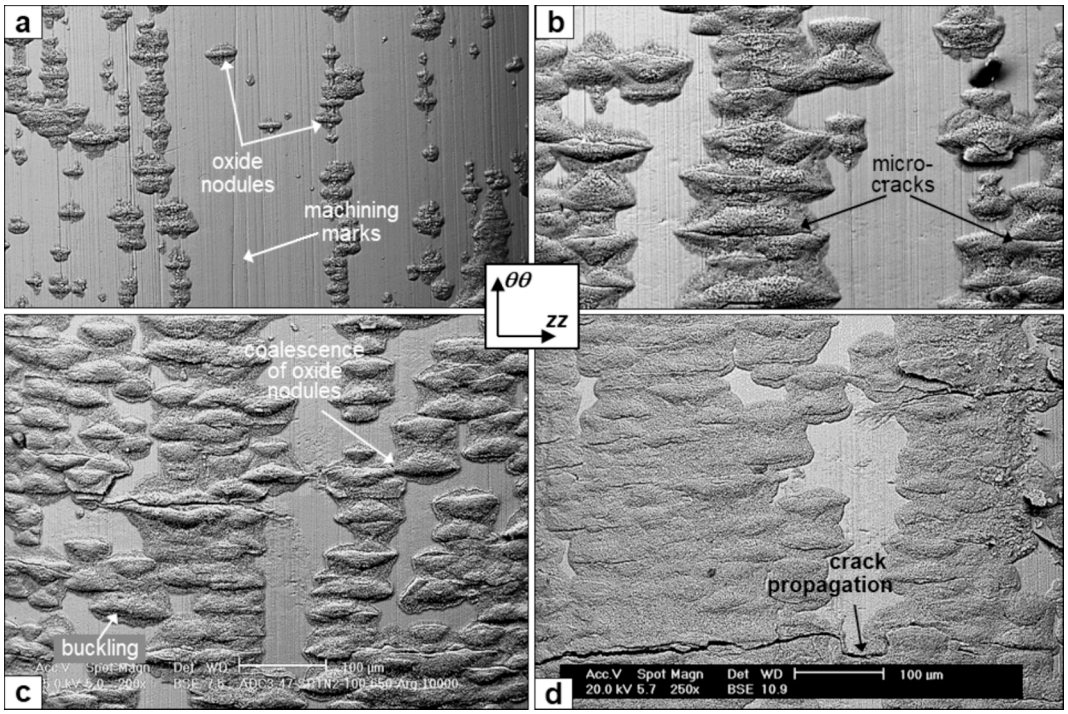

Fig. 8. Growth of the oxide layer under argon, by nucleation, lateral growth and coalescence of oxide nodules after increasing numbers of TF cycles: **a)** 5,000, **b)** 7,500, **c)** 10,000 and **d)** 12,500 cycles.

surface, an evolution in the shape of these oxide nodules was observed during cycling, from an initially approximately circular shape to a "diamond" shape (Fig. 8a). In fact, this shape would result from oxide growth accelerated by lateral propagation of micro-cracks along *zz* direction. Up to the first thousand cycles, only a very small fraction of the specimen surface showed such an oxidation pattern, but as the number of TF cycles increased, the oxide islands grew (Fig. 8b), coalesced (Fig. 8c) to end up covering almost the entire surface (Fig. 8d).

After a few thousand cycles, some of the oxide islands were buckled and crossed by several superficial micro-cracks propagating perpendicular to *θθ* (Fig. 8b). These micro-cracks were undoubtedly linked to the shape transformation of the oxide nodules, leading to preferential oxygen diffusion along *zz* (i.e. perpendicular to the main stress). By increasing the number of cycles, some micro-cracks coalesced from island to island, following a zig-zag path (crystallographic) through the non-oxidized zones (Fig. 8c-d and Fig. 9a). Post-mortem micrographs of the specimen in cross-section indicated that the cracks propagated in depth into the steel following a tortuous path, roughly along *zz* direction. At the macroscopic scale, the crack propagation was perpendicular to *θθ*. In-depth cracks appeared less open (with a thinner crack tip) than in air, but again filled with oxide (Fig. 9b).

4.3. Nitrogen

Observations in cross-section revealed a very porous and stratified oxide scale with alternating layers of magnetite and spinel, and a very thin surface layer of hematite (Fig. 10a). Its total thickness was about 10 μm after 40,000 cycles (i.e. thinner than in air or argon at 30,000 cycles). At the interface with the steel, areas of local delamination were revealed. The irregularity of this interface could indicate heterogenous oxidation (i.e. preferentially intergranular and inter-martensitic). An acicular morphology with a tangle of thin hematite whiskers was observed at a finer scale of observation on the oxide surface (Fig. 10b).

Although such an oxide layer did not cover the whole surface of the specimen, it appeared more uniform than the layer formed under argon. A preferential oxide growth could be observed on the initial polishing

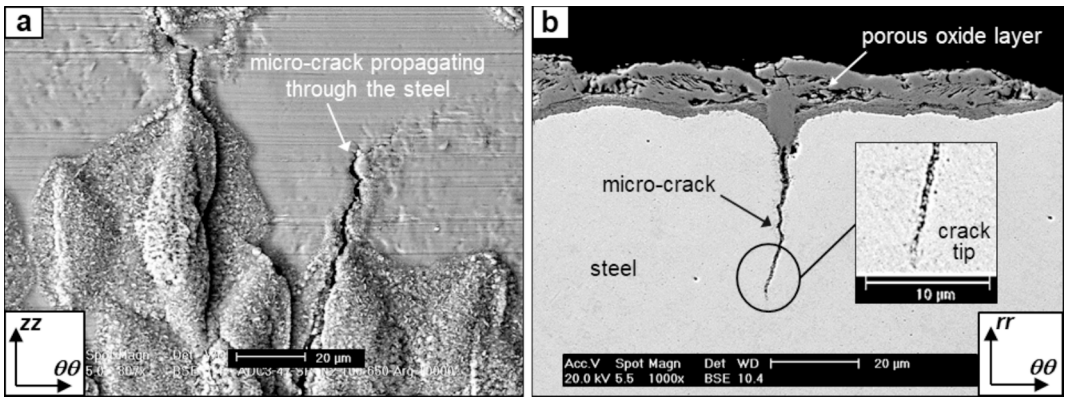

Fig. 9. Propagation of a micro-crack in the steel observed on the specimen after 30,000 TF cycles in argon, in surface **(a)** and in-depth **(b)**.

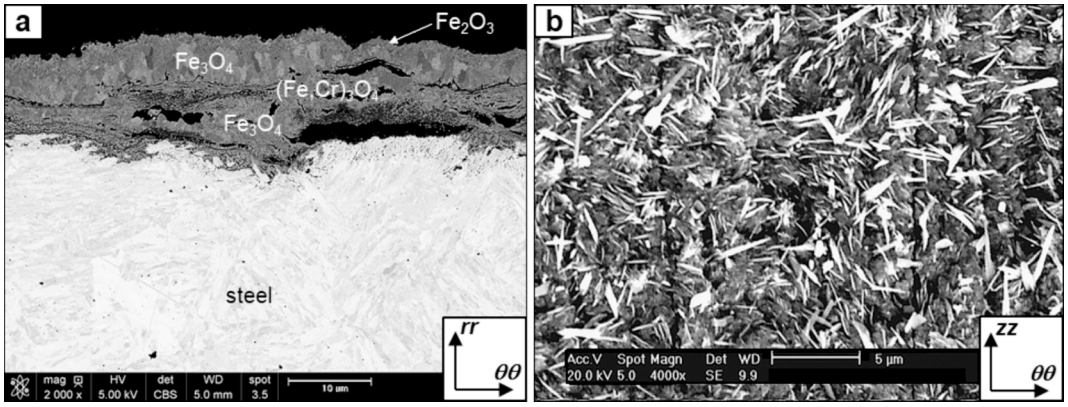

Fig. 10. Oxide layer formed in nitrogen after 40,000 TF cycles: **a)** stratified and porous structure observed in cross-section**; b)** acicular structure with thin hematite whiskers in surface.

grooves, which ended up cracking under thermo-mechanical loading (Fig. 11a). Local areas of buckling or spalling were also highlighted, which could explain the stratified structure of the oxide (Fig. 11b).

In cross-section, most of the micro-cracks appeared particularly thin, with a sharp crack tip. The oxygen diffusion led to an intergranular and inter-martensitic oxidation of the crack lips. The micro-cracks were superficially filled by oxide and presented a "V-shape" on a few micrometres in depth (Fig. 12a). Unlike tests in air and under argon, no specific periodic micro-cracking (heat checking) was observed on the oxide surface up to 40,000 TF cycles. This likely reveals the ability of the oxide layer to self-accommodate the $\theta\theta$ strain rather than cracking uniformly. However, fairly marked surface micro-cracks were observed locally (Fig. 12b).

5. Discussion

5.1. Oxidation

During TF tests, the thermal transients experienced by the steel led to a cyclic oxidation, whose kinetics and oxide morphology changed depending on the exposure time and temperature (as evidenced by the oxidation gradient observed on the external surface of the specimen in Fig. 2a). The effect of the temperature on the kinetics of parabolic oxidation in air was previously modelled, for thermal cycles between

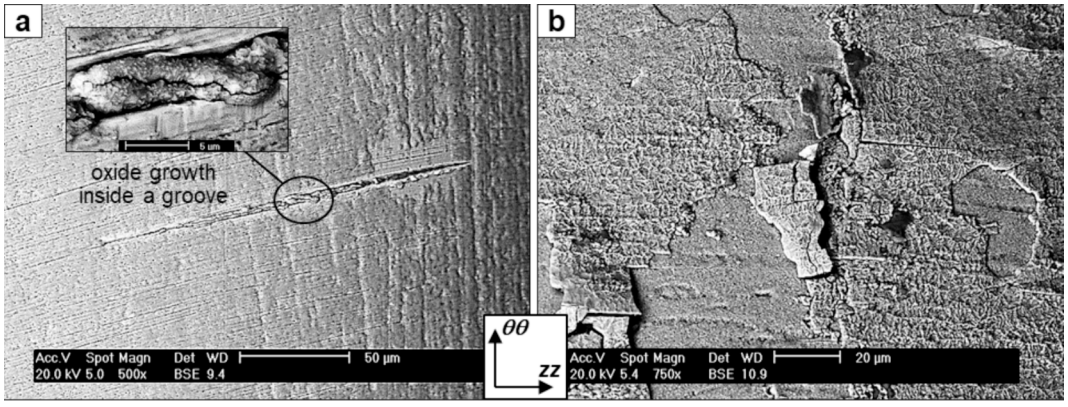

Fig. 11. a) Thin oxide film formed on the surface of the specimen after 10,000 TF cycles in nitrogen (the brighter areas correspond to the steel substrate); **b)** local spallation of the superficial oxide layer.

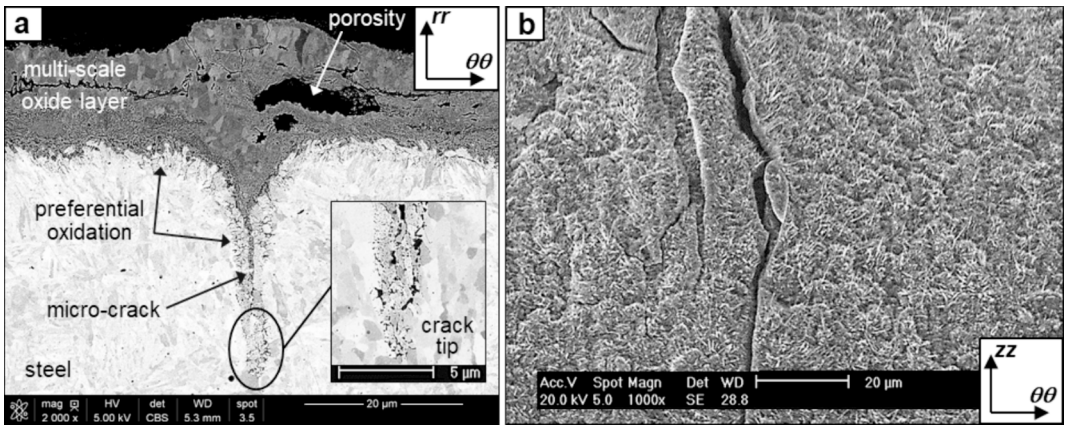

Fig. 12. Cross-section of a specimen tested in nitrogen after 40,000 TF cycles, showing a micro-crack propagation in-depth **(a)**; micro-crack initiation in surface of the oxide layer **(b).**

100 °C and various T_{max} ranging from 500 and 685 °C [55]. The present investigation further reveals that the oxidation kinetics also depends on the test environment. But despite the strong reduction in PO_2 under inert atmospheres, an oxide layer was always observed, with a thickness however lower under argon and especially under nitrogen than in air.

The environmental conditions of the TF test also impacted the coverage and morphology of the oxide layer, namely:

- quite homogeneous and compact layer in air;
- rather compact and localized ("nodular or "island-type") oxidation under argon;
- porous, relatively thin and fairly non-uniform layer under nitrogen.

Identical oxide phases, i.e. hematite (Fe_2O_3), magnetite (Fe_3O_4) and spinel ($(Fe,Cr)_3O_4$), were observed regardless of the test atmosphere. A thermodynamic simulation by Thermocalc® software (using the TCFE8 base) shows that the equilibrium PO_2 at the Fe_2O_3/Fe_3O_4 interface is less than 10^{-13} bar. The PO_2 in our test environments are much higher and therefore sufficient to allow the formation of these two phases. This is confirmed by EDX mapping, showing the distribution of the main oxide elements and clearly highlighting the interfaces between the different oxide compounds and with the steel (Fig. 13). A thin spalled layer of spinels can also be observed inside the magnetite layer. The oxygen diffusion paths from surface micro-cracks through the oxide layer could also be distinguished. It should be noted that wüstite (FeO), supposed to form under the inner magnetite layer above 570 °C according to the Fe-O equilibrium diagram [56–58], was never observed on our test specimens. As reported in [56], the presence of 5 % chromium in the steel, by increasing the wüstite formation temperature to 850 °C, did not allow its formation at the temperature levels at which the steel was exposed (T_{max} = 650 °C). Also, Balasko et al. [58] revealed the presence of wüstite in the internal oxide layer of a soft annealed AISI *H*11 tool steel

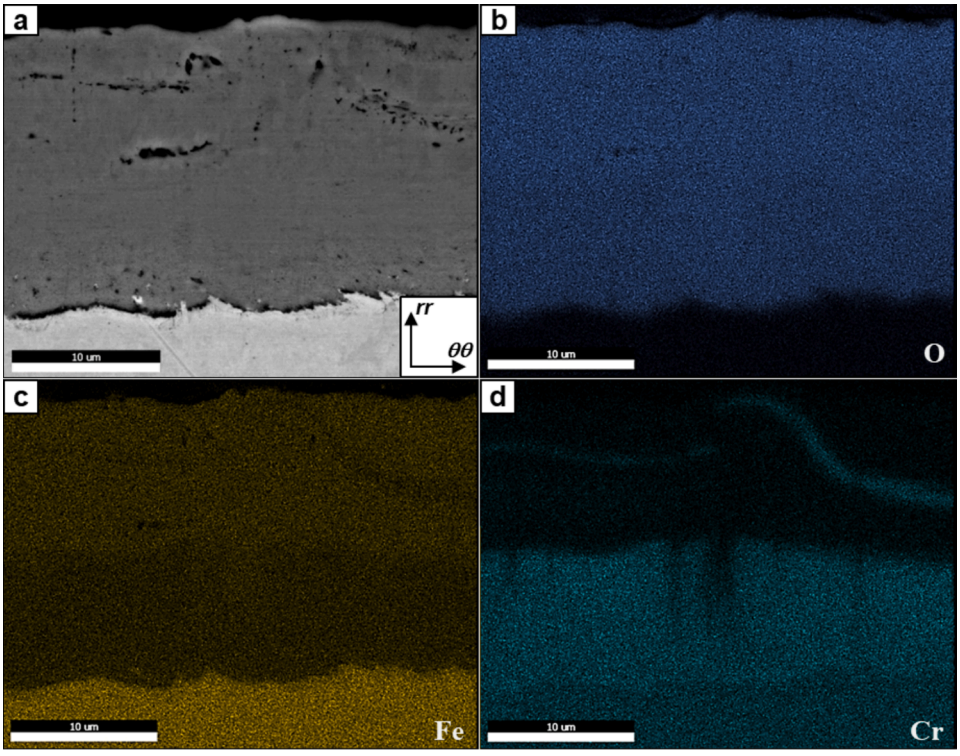

Fig. 13. SEM micrograph (BSE mode) of the oxide layer formed in air **(a)**, and associated EDX elemental maps of oxygen **(b)**, iron **(c)** and chromium **(d)**, revealing the interfaces inside the oxide layer and with the steel.

after an aging test at 700 °C, while wüstite was absent at this temperature in the hardened and tempered samples.

Detailed cross-sectional observations revealed relatively compact and adherent magnetite and spinel layers in air (and to a lesser extent under argon), whereas they were much more porous and/or "damaged" (stratified oxide scale resulting from successive spallations) under nitrogen. A columnar structure with large grains was highlighted in the magnetite. The inward and outward growth of the oxide layer could be clearly highlighted under argon, the original surface of the steel being visible in the non-oxidized zones, on either side of the oxide nodules (Fig. 7a). The formation of magnetite and hematite was driven by a cationic mechanism (oxidation at the environment/oxide interface, by diffusion of iron towards the surface), while an anionic mechanism led to the growth of the $(Fe,Cr)_3O_4$ spinel layer (oxidation at the oxide/steel interface, by diffusion of oxygen through the oxide into the steel).

Additional XRD analyses (Fig. 14) revealed a higher amount of hematite formed in air compared to lower PO_2 atmospheres, as previously highlighted by SEM observations in cross-section (Fig. 4a, 7a and 10a). This was also reported by Min et al. [59] under isothermal oxidation of a similar steel grade, which explained the preferential formation of hematite by thermodynamic considerations (based on calculations with the ThermoCalc® software). XRD spectra also revealed a greater proportion of magnetite under nitrogen than in other atmospheres (argon, and especially air). However, this was not consistent with cross-sectional post-mortem micrographs (Figs. 10, 15a and b). In fact, we believe that the thinness of the hematite layer above the magnetite layer could amplify the intensity peak of magnetite measured by XRD on TF specimens tested under reduced PO_2. The preferential growth of the magnetite in air would be due to higher oxygen content in the test atmosphere, combined to a better adherence of the oxide scale to the parent steel and the Fe-ion diffusion outward, that could consequently enhance the magnetite growth rate [60]. Under argon and especially under nitrogen, it was indeed found that the oxide layer was much less adherent (with large voids at the oxide-steel interface) than in air.

It should be emphasized that whatever the test atmosphere – and therefore the homogeneity of the oxide layer – TF micro-cracks initiated exclusively in the oxide scale, and more particularly in the surface hematite layer and magnetite underlayer (Fig. 15a). Local spalling of the oxide layer was also observed near the micro-cracks present in the oxide islands under argon. The same oxidation sequence as on the surface was observed inside the cracks in the steel, namely a growth of the external oxides by diffusion of iron through the micro-cracks, and of the internal oxide by diffusion of oxygen. The micro-cracks, by leading to the creation of new non-oxidized surfaces, activated the formation of new quantities of oxide. The successive spallation of the oxide multilayer under TF cycling could explain the stratified structure of the oxide layer and the irregularity of the internal oxidation front under argon and nitrogen. This delamination was probably promoted by the decohesion of the oxide and the large defects (porosities) present at the oxide-steel interface (Fig. 15b).

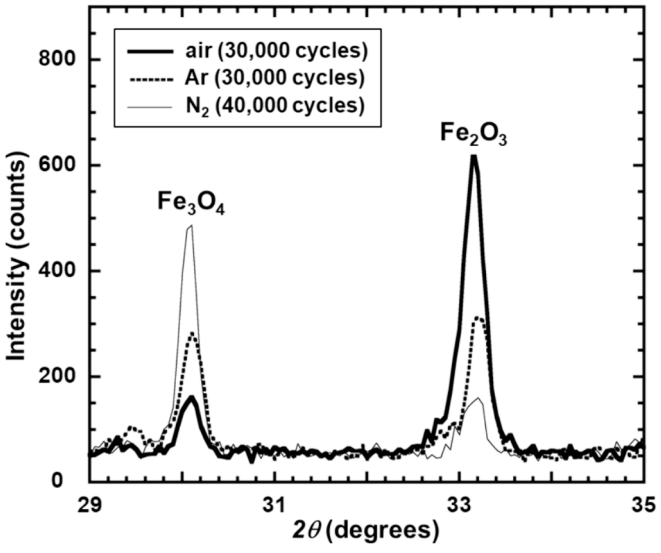

Fig. 14. XRD patterns showing the effect of the test environment on the hematite / magnetite proportion in the oxide layer formed after consequent TF cycles.

5.2. Superficial damage

In air, the damage mechanisms resulting from thermal cycling can be decomposed into the following successive stages during increasing TF cycles, as illustrated in Fig. 16a:

a-1) growth of a multi-layered and compact oxide on the steel surface, by a temperature-activated diffusional process;

a-2) formation of a periodic surface micro-crack network (propagating through the oxide perpendicular to the $\theta\theta$ axis and parallel to zz and rr axis), leading to oxidation growth on a few micrometres into the steel (by diffusion short-circuit through micro-cracks);

a-3) stopping and healing of certain micro-cracks at the interface with the steel; in-depth propagation of other cracks, leading to subsequent swelling of the crack lips on the surface (due to oxide preferential growth) and steel depletion of the steel along the cracks (by diffusion in the blunt zones);

a-4) propagation of main cracks deeper into the steel following a straight path, and disappearing of "secondary" surface micro-cracks by oxide healing (due to the oxide scale growth).

The oxide growth occurred mainly during the hot phases of the TF cycles [55], i.e. when the steel was subjected to thermo-mechanical compressive stresses (Fig. 3). During the cooling phase, the "composite" oxide layer found itself in tension when the steel was subjected to thermo-mechanical tensile strain, leading to cracking (by formation of a heat-checking network). A uniaxial network was here observed because the strains/stresses prevailing in the specimen were uniaxial (major loading axis along $\theta\theta$). Note that on another specimen geometry involving a bi-axial mechanical loading, the resulting heat-checking network was biaxial [17]. As previously explained, the through-scale cracking of the multilayer oxide scale was caused by the thermal expansion mismatch between the superficial layer and the steel substrate of different expansion coefficients, under the effect of the thermal gradients of maximum amplitude at the end of cooling (Fig. 3). It should be noted that the same type of cracking was observed on specimens coated with intermetallic compounds and tested in air under two loading conditions (biaxial and uniaxial) [51]. Heat-checking would thus be a specific damage of the ductile steel in the presence of a compact, adherent and hard (oxide or intermetallic) coating. By opening and propagating, the micro-cracks contributed to accelerate the oxide growth by short-circuit diffusion, and to disrupt the oxide/steel interface by formation of local oxide excrescences (as previously highlighted on micrographs of Fig. 6a and b).

The crack healing observed in air has also been reported in the literature, for example in NiO scales formed on Ni99.2 oxidized at 800 °C and in Cr_2O_3 scales on an alloy 800 subjected to creep at 800 °C and various strain rates [56]. Schütze proposed two different mechanisms of healing: a first process (by metal cation diffusion) restoring the protective oxide scale, and a second one (by oxygen anion diffusion) increasing local inward growing oxide into the metal. Schütze also suggested the existence of a critical deformation rate, $\dot{\varepsilon}_c$, below which the protective action of the scale would be restored. A previous study [17] has revealed that the strain rate imposed in our TF experiments ($10^{-4} < \dot{\varepsilon} < 10^{-3}$) was considerably higher than in the creep experiments ($10^{-8} < \dot{\varepsilon} < 10^{-6}$) reported in [56], and therefore higher than $\dot{\varepsilon}_c$. This situation explains the propagation of cracks in the metal, as

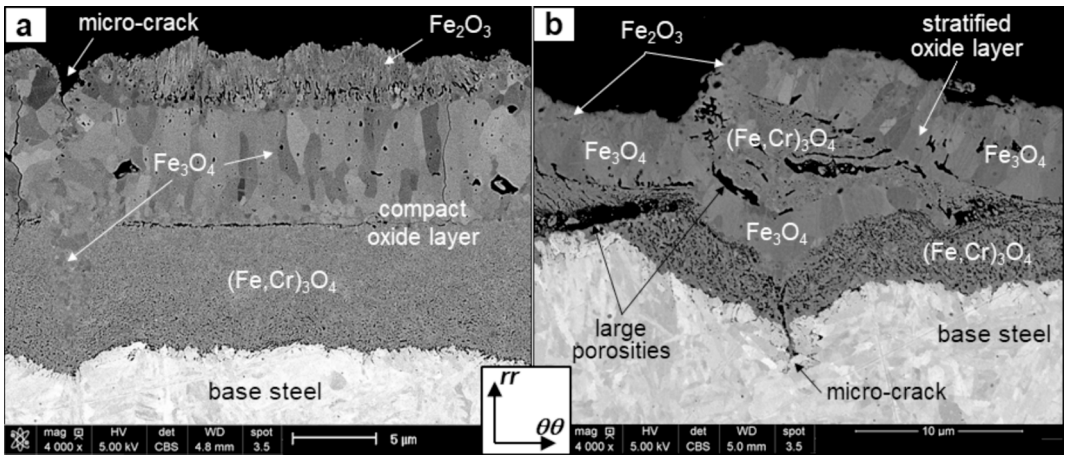

Fig. 15. Detailed micrographs of the oxide layer formed in air **(a)** and under argon **(b)**, showing differences in structure and compactness.

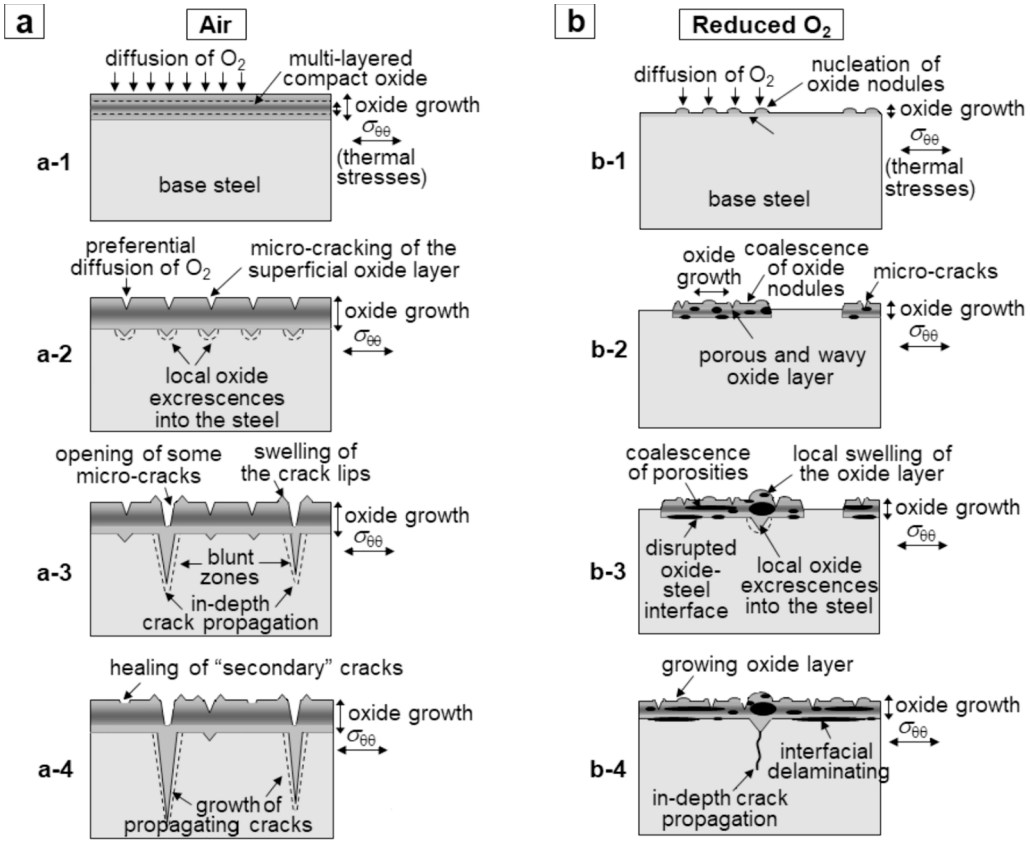

Fig. 16. Mechanisms of micro-crack initiation and propagation under increasing numbers of TF cycles: oxidation-assisted propagation in ambient air **(a);** reduced and delayed propagation in low PO_2 atmosphere **(b)**.

previously illustrated in Fig. 6a showing that the superficial network of micro-cracks was almost entirely replicated in-depth. The chemical composition of the base-steel was locally altered by oxidation in the blunt zones, especially at the crack tip (Fig. 6b) and along the internal "free surfaces" of the steel.

The propagation of micro-cracks in the steel induced a redistribution of the force lines, concentrating the stresses at the tip of the longer micro-cracks. In a first step, these micro-cracks propagated by a fatigue-oxidation mechanism, with a propagation speed increased by the diffusion of oxygen, weakening the steel around the crack tip (and even more so as the crack was open in surface). By propagating, macro-cracks annihilated the progression of neighbouring micro-cracks by redistributing local stresses along the force lines (Fig. 16a-4).

Under reduced PO_2, damage mechanisms appeared with different sequencing and dynamics during TF cycling (Fig. 16b):

b-1) slow growth of a heterogeneous and porous oxide, starting by local nucleation of oxide nodules under argon and micro-buckling of the oxide nodules;

b-2) coalescence of oxide nodules leading to an increase in the covering of the steel surface, while micro-cracks initiated perpendicular to $\theta\theta$ axis in the thickest oxide nodules;

b-3) coalescence of nearby micro-cracks in surface and of porosities in the oxide layer, leading to local swelling of the oxide (due to underlying cavities), disruption of the oxide/steel interface and local oxide

penetration into the steel (due to iron diffusion);

b-4) delamination of the oxide/steel interface and crack propagation into the steel, following a zig-zag path.

Under argon as under nitrogen, the oxide was thinner due to the lower oxygen partial pressure in the test atmosphere. As the micro-cracks were first confined to "oxide islands" under argon (PO_2 = 4x10^{-3} mbar), the surface micro-crack (heat checking) density was reduced, especially at the beginning of the cycling (Fig. 8b). Under nitrogen (PO_2 = 1x10^{-5} mbar), the very thin and non-uniform oxide layer formed on the surface was cyclically and locally damaged by spallation. Discussing the behavior of oxide scales on 2.25Cr-1Mo steel during thermal cycling, Christl et al. attributed the oxide scale buckling (and the subsequent formation of hematite whiskers) to highly compressive stresses of the new oxide formed at the magnetite-hematite interface (with cationic and anionic opposite diffusion in both oxide scales) [60]. Under highly reduced PO_2, the low compactness and adhesion of the oxide layer with the steel substrate has a consequence on damage mechanisms. Numerous internal porosities or cavities, maybe formed as a result of iron ions diffusion in the magnetite layer, contributed to initiate the oxide layer delamination (Fig. 10a, Fig. 12a and Fig. 15b). Under shear stresses, those porosities coalesced, leading to cyclical spalling and preventing at the same time in-depth oxidation and micro-crack propagation. Indeed, the undulations observed on the surface of the oxide layer (Fig. 10a and Fig. 15b) could reflect the cumulative compressive strain (creep type) felt by the substrate.

In a reduced PO_2 atmosphere, the cracks propagating into the steel exhibited a thinner crack tip and a shallower depth than in air, suggesting that the propagation was much less assisted by oxidation. Indeed, EDX elemental mapping revealed zones of iron depletion and preferential chromium oxidation around the oxidized surface of the steel and the crack lips (Fig. 17). On the other hand, the cracks followed a saw-tooth like path, whether on the free surface of the steel (Fig. 8c–d) or in depth (Fig. 9b and Fig. 12b), reflecting a crystallographic mechanism for crack propagation. A few isolated cracks ended up propagating deeper over a very large number of TF cycles, when the plastic deformation accumulated by the specimen reached a high level (by the so-called "cyclic softening" phenomenon, as will be discussed in the next section).

5.3. Crack propagation in steel

At the macro-scale and whatever the test environment, macro-cracks propagated perpendicularly to the circumferential $\theta\theta$ axis, both in surface (Fig. 18a-c) or in depth (Fig. 18d-e). However, a much more sinuous propagation path was observed under argon and nitrogen (Fig. 18b-c and e), and even under air beyond a critical depth (around 2 mm) corresponding to the areas subjected to relatively low temperatures during the TF test. Under reduced partial pressure of oxygen, macro-cracks initiated at different sites, with initially asymmetric propagation (on the curvature radius). These cracks ended up joining together (by coalescence) to form a single macro-crack (Fig. 18b and c).

The crack propagation curves exhibited a typical sigmoidal evolution, whatever the test atmosphere (Fig. 19a). Macro-crack initiation was strongly delayed under reduced PO_2. For instance, the crack initiation life of the specimen under nitrogen was almost thrice as long as in air. In addition, decreasing PO_2 could help reduce the growth rate of macro-cracks in the early stages (where the temperature was high). The EDX elemental maps carried out on the post-mortem specimen tested in air showed the formation of chromium oxide by oxygen diffusion and the iron depletion of the steel in the blunt zone around the crack tip (identically to what was observed previously on the external surfaces), attesting to the influence of oxidation on crack propagation (Fig. 20). This effect could be quantified using destructive tests with an intermediate number of cycles. Several studies have highlighted the effect of

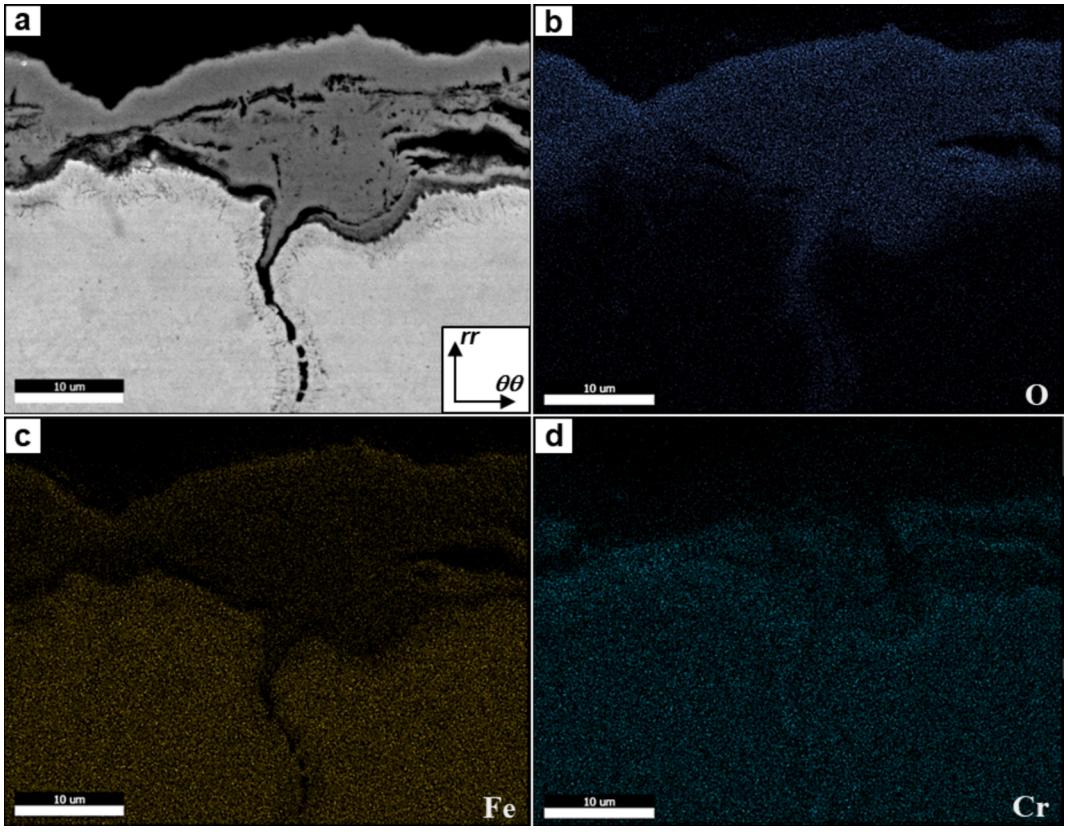

Fig. 17. SEM micrograph (BSE mode) of the oxide layer with a micro-crack under nitrogen **(a)**, and associated EDX elemental maps of oxygen **(b)**, iron **(c)** and chromium **(d)**.

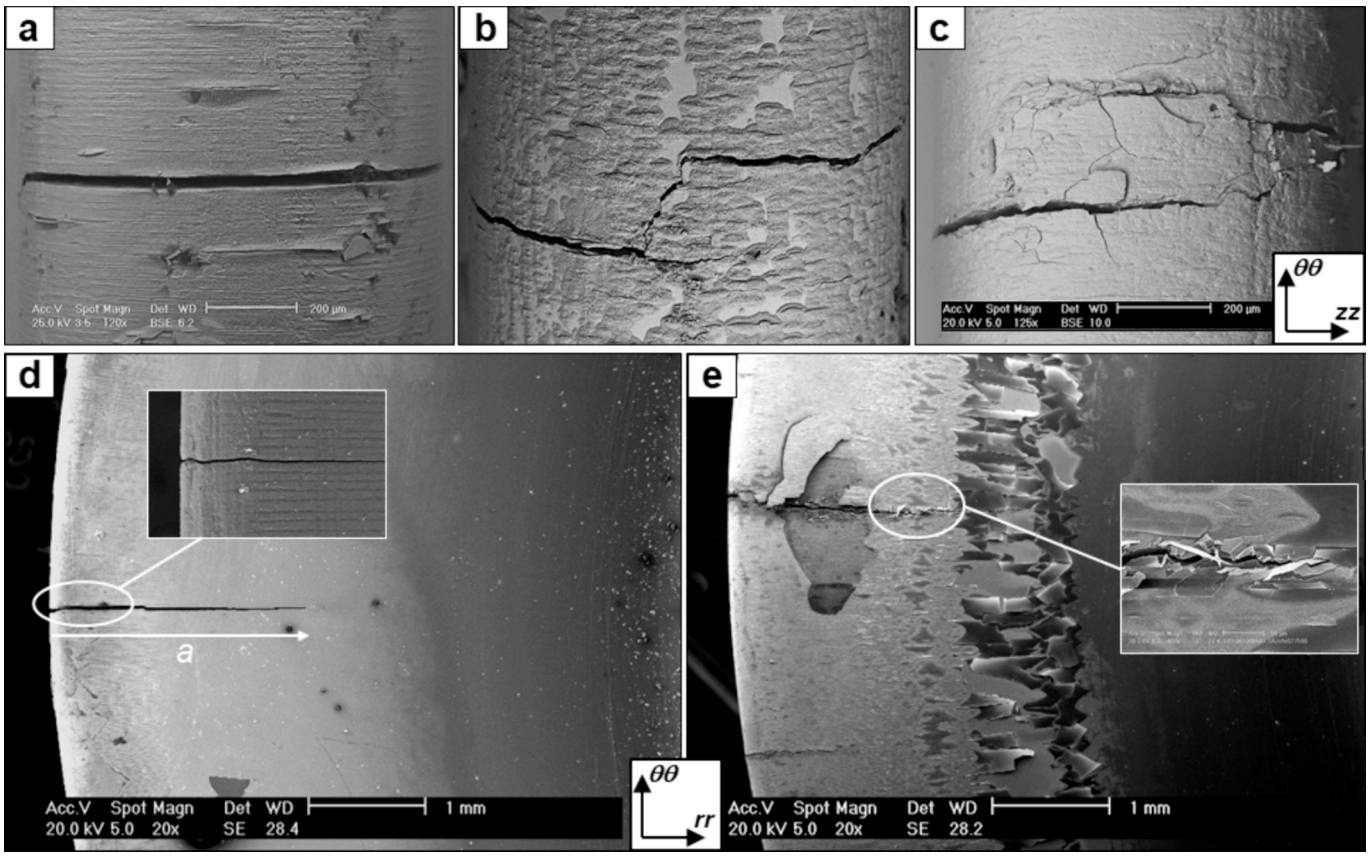

Fig. 18. Macro-cracks observed on the top surface of the specimen, after: **a)** 10,000 TF cycles in air, **b)** 15,000 cycles under argon, c) 27,500 cycles under nitrogen; In-depth macro-crack propagation after: **d)** 20,000 cycles in air, **e)** 35,000 cycles under nitrogen.

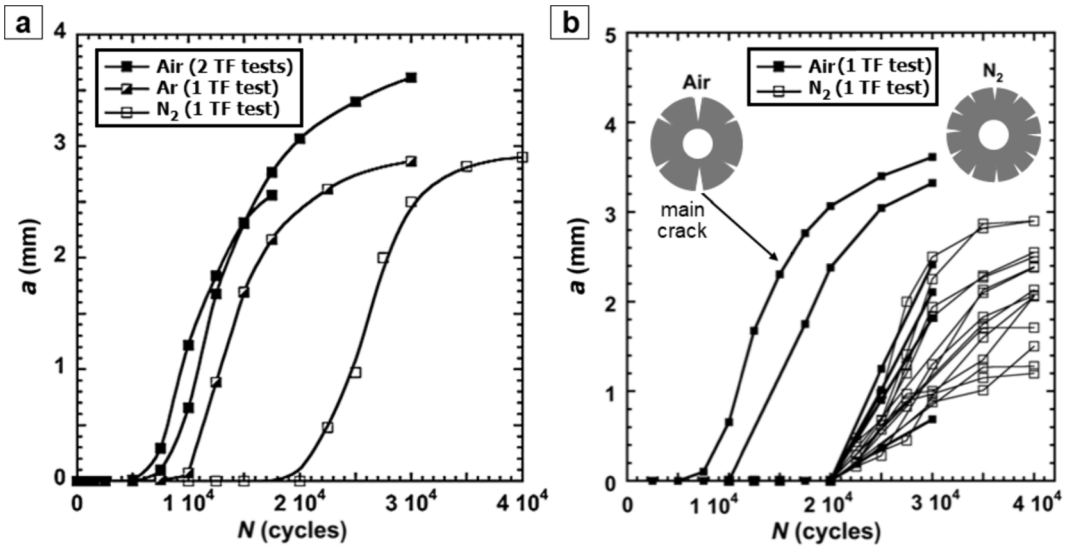

Fig. 19. Aa) Effect of the test atmosphere on the TF life of X38CrMoV5 steel; **b)** Propagation curves of all main cracks in air and under nitrogen (the position of the macro-cracks measured on the disc are indicated schematically above the curves).

environment in crack propagation by the formation of oxides or intermetallics inside the cracks [16,32–34]. Sjöström et al. emphasized the effect of these hard compounds to prevent the crack closure and thus accelerate their propagation [16]. In addition, cracks propagate more quickly through the brittle oxides and intermetallic than through a ductile steel.

Two main cracks, diametrically opposed, started prematurely under air and argon, respectively at 7,500 and 10,000 cycles (Fig. 19a). These cracks, called "main" cracks, reached depths greater than 3 mm under air (and less under argon). Later (around 20,000 cycles), several "secondary" cracks uniformly distributed on the disk propagated simultaneously (Fig. 19b). The competition between these multiple macro-cracks slowed down the propagation of the main cracks, which were also hampered by the reduction in the stress intensity factor along *rr*

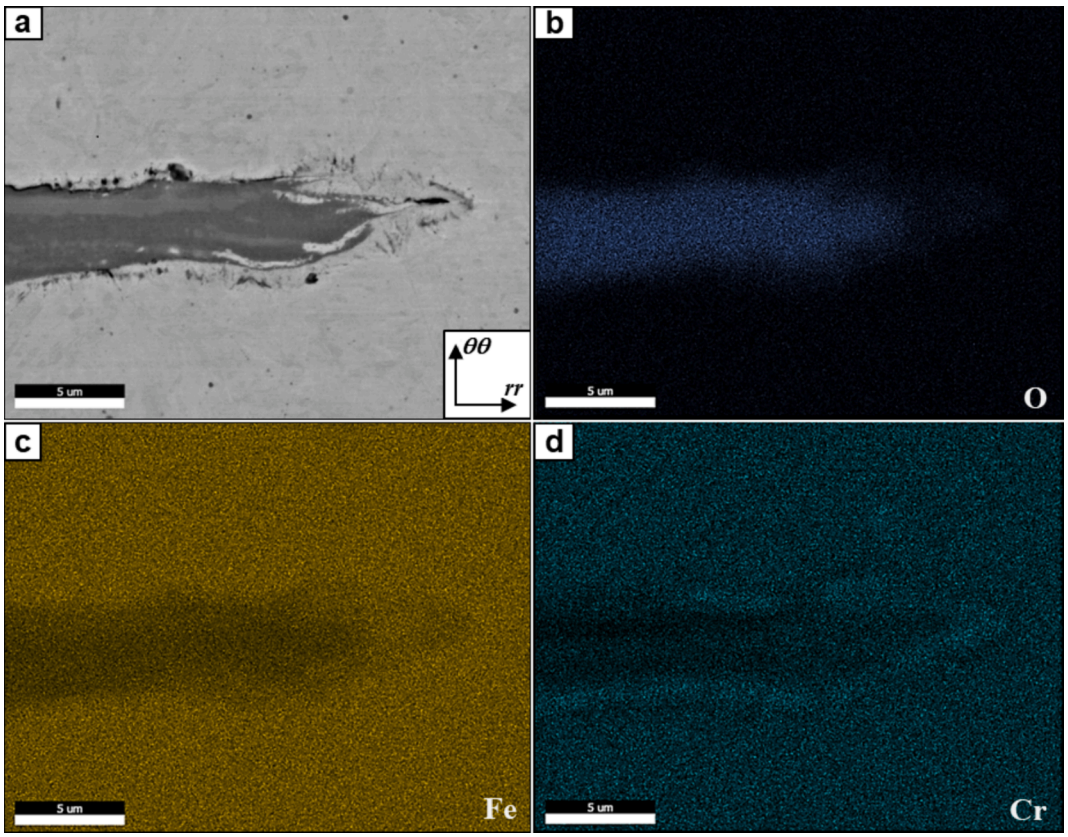

Fig. 20. SEM micrograph (BSE mode) of a crack tip in air **(a)**, and associated EDX elemental maps of oxygen **(b)** and chromium **(d)** and the iron depletion in the blunt zone **(c)**.

(zones of lower stress, due to a low thermal gradient). Under nitrogen, several macro-cracks uniformly distributed around the disk started simultaneously at 20,000 cycles (Fig. 19b). This number of cycles would correspond to the intrinsic fatigue limit of the steel. It should be noted that when the specimen presented a surface cracking network (in air or under argon), two main cracks started first, then all secondary cracks started at a similar number of cycles (around 20,000 cycles). This was also observed with TF specimens covered with an intermetallic layer [51]. In fact, by concentrating the stress field, the micro-cracks forming the superficial heat-checking network led to a local amplification of the stresses at the tip of the cracks in-depth. This concentration of stresses, assisted by oxidation, was responsible for the local reduction in the life span of the steel, as manifested by the growth of two diametrically opposed main cracks.

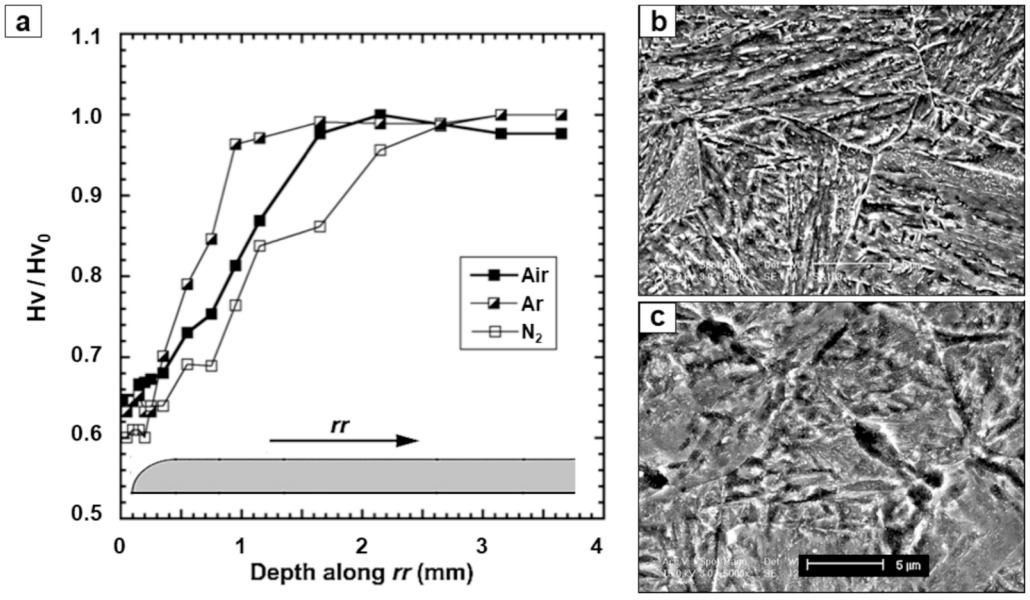

Fig. 21. Aa) Drop in hardness in depth of the post-mortem specimens after a TF test in air, argon and nitrogen, after the TF test, indicating the softening of the steel; **b)** initial martensitic microstructure of the steel; **c)** bainitic microstructure observed after the TF test.

Numerous works on HWTS, tested either in TF, LCF or TMF, have reported that the combined thermal and thermo-mechanical loadings decreased the mechanical properties of the steel by deconsolidation and softening [2,7,8,14,61–64]. This was also observed in isothermal and anisothermal tempering experiments [58,64–66]. These studies showed that the softening was more significant as the temperature and stress level were high. Thermal loading, particularly close to the tempering temperature (605 °C), also contributed to this softening phenomenon (either cyclic or static) [66]. Indeed, Fig. 21a shows a progressive drop in micro-hardness in the upper part of the post-mortem TF specimens, from the surface up to about 2 mm in depth. The rate of loss of hardness, decreasing with depth, was relative to the levels of thermal and thermo-mechanical stresses suffered by the steel. This was also attested by the modification of the microstructure of the steel, initially composed of fine martensitic laths with very fine carbides (Fig. 21b) and a Vickers hardness of 485 Hv (after the heat treatment), which became bainitic with much coarser carbides (Fig. 21c) and approximately 350 Hv at the end of the TF cycling. Mebarki et al. also reported this microstructural evolution induced by tempering and isothermal fatigue on the same tool steel [66]. They highlighted an increase in the size of secondary carbides by coalescence and a decrease in the dislocation density, based on finer scale TEM observations. Although the test atmosphere a priori has no effect on thermal stresses, the presence of micro-cracks in air and under argon, by amplifying the stress fields at the crack tips (concentration zones), could accelerate the weakening of the mechanical properties of the steel (Fig. 21a). This phenomenon is amplified by oxidation, which locally modifies the composition of the steel, particularly in the blunted zones around cracks.

Depending on the nature of the surface – itself conditioned by the environment – two types of macroscopic damages can therefore be distinguished:

Damage by TF/environment coupling (in the presence of compact and well adherent layer or multilayers, such as oxide or intermetallics coatings), including a superficial micro-cracking step characteristic of the TF cracking of hard surface layers, followed by macroscopic crack propagation from micro-cracks when exceeding locally the cracking resistance of the substrate (depending on the oxide behaviour, the size of surface micro-cracks and the properties of the steel underlay). In this mode, oxidation can be considered as an accelerating factor in the growth of surface and in-depth cracks, reducing the TF life of the steel.

Intrinsic damage by TF (in the case of a mono-material), manifesting on the macroscopic scale by multiple and simultaneous cracks initiated on the surface (and sometimes inside the material), and by localization of plastic deformations as soon as the fatigue resistance of the material has been achieved. In this mode, cracking can be considered as the consequence of a cyclical thermo-mechanical softening process of the steel, the mechanical properties of the steel being considerably degraded by microstructural transformations due to stresses (and in particular to temperature).

6. Conclusion

TF tests were performed on X38CrMoV5 tool steel between 100 °C and 650 °C in air, argon and nitrogen (after primary and secondary vacuum), in order to assess the effect of the partial pressure of oxygen on the damage mechanisms.

A FEM analysis revealed uniaxial thermo-mechanical cyclic loading on the top of the specimen, with alternating compression/tension. In the stabilized regime, the maximum tensile stress was reached at the minimum temperature of the TF cycle, and the maximum compressive stress at the maximum temperature.

An oxide multilayer, composed of hematite (Fe_2O_3), magnetite (Fe_3O_4) and spinel ($(Fe,Cr)_3O_4$), was identified in all TF conditions. This oxide layer was however thinner under reduced oxygen partial pressure. In air, a uniform and compact oxide, well adherent to the substrate, was formed. Under argon, a heterogeneous “island-type” oxidation was observed, starting by nucleation of isolated oxide nodules coalescing as the number of TF cycles increased. When the oxygen partial pressure was further reduced (under nitrogen), a thin and very porous oxide layer, slightly adherent to the steel, was highlighted.

Depending on the structure of the oxide layer, different modes of surface damage were highlighted. A set of parallel micro-cracks initiated perpendicular to the hoop stress after a few thousand TF cycles on the oxide layer formed in both air and argon, with however lower density in argon due to localized and slowed oxide growth. Under nitrogen, a strong spallation occurred locally, resulting from the relief of high compressive stresses in the particularly porous and poorly adherent oxide layer.

Two types of macro-cracking mechanisms were highlighted depending on the test atmosphere. In air, a damage by TF/environment coupling occurred, in which crack initiation and propagation were accelerated by oxidation. The composition of the steel was locally modified by oxidation, and its mechanical properties weakened by stress concentration around propagating cracks. Under reduced oxygen partial pressure, an intrinsic damage by TF (in the absence of surface micro-cracks), due to cumulated plastic strain and cyclical thermo-mechanical softening of the steel. Consequently, the TF lifespan was greatly increased by a strong reduction in the oxygen content in the environment, although oxidation was not completely prevented.

CRediT authorship contribution statement

M. Salem: Writing – original draft, Resources, Methodology, Investigation, Formal analysis, Data curation, Conceptualization. **S. Le Roux:** Writing – original draft, Investigation, Data curation. **G. Dour:** Writing – review & editing, Project administration, Methodology, Funding acquisition, Formal analysis, Conceptualization. **A. Vande Put:** Writing – review & editing.

Declaration of competing interest

The authors declare that they have no known competing financial interests or personal relationships that could have appeared to influence the work reported in this paper.

Data availability

Data will be made available on request.

Acknowledgments

The authors would like to thank Aubert & Duval Holding for providing the investigated material.

References

[1] Fuchs KD. Hot-work tool steels with improved properties for die-casting applications. In: Proc. of 6th International Tooling Conference; 2002. p. 15–22.
[2] Pellizzari M, Molinari A, Cescato D, Ghidini A, Cantini S. Thermal fatigue properties of hot-work tool steels. Int J Microstruct Mater Prop 2008;3(2–3): 363–72. https://doi.org/10.1504/IJMMP.2008.018772.
[3] da Silva Jr RR, Totten GE, Vendramim JC, de Campos L, Canale F. Thermal Fatigue in Hot Work Tool Steels - A Review. In: Proc. of 29th ASM Heat Treating Society Conference, Columbus, Ohio (USA), Paper No: ht2017p0457; 2017. p. 457-68. Doi: 10.31399/asm.cp.ht2017p0457.
[4] Solgi P, Chenarani M, Reza Eivani A, Ghosh M, Kumar V, Reza JH. Heat checking as a failure mechanism of dies exposed to thermal cycles: A review. J Mater Res Technol 2023;26:865–95. https://doi.org/10.1016/j.jmrt.2023.07.170.
[5] Starling CMD, Branco JRT. Thermal fatigue of hot work tool steel with hard coatings. Thin Solid Films 1997;308:436–42. https://doi.org/10.1016/S0040-6090(97)00600-7.
[6] Persson A, Hogmark S, Bergström J. Simulation and evaluation of thermal fatigue cracking of hot work tool steels. Int J Fatigue 2004;26(10):1095–107. https://doi.org/10.1016/j.ijfatigue.2004.03.005.
[7] Persson A, Hogmark S, Bergström J. Thermal fatigue cracking of surface engineered hot work tool steels. Surf Coat Technol 2005;191(2–3):216–27. https://doi.org/10.1016/j.surfcoat.2004.04.053.

[8] Ebner R, Marsoner S, Siller I, Ecker W. Thermal fatigue behavior of hot work tool steels: heat check nucleation and growth. Int J Microstruct Mater Prop 2008;3 (2–3):182–94. https://doi.org/10.1504/IJMMP.2008.018726.

[9] Muhič M, Tušek J, Kosel F, Klobčar D, Pleterski M. Thermal fatigue cracking of die-casting dies. Metalurgija 2010;49(1):9–12. https://hrcak.srce.hr/40242.

[10] Klobčar D, Kosec L, Kosec B, Tušek J. Thermo fatigue cracking of die casting dies. Eng Fail Anal 2012;20:43–53. https://doi.org/10.1016/j.engfailanal.2011.10.005.

[11] Suzuki M, Ishihara M, Miyachi H. Residual Stress and Heat Checking in Die Casting Dies. In: Transactions of the North American Association (NADCA) Congress and Exposition, SDCE Paper 6472; 1972.

[12] Malm S, Svensson M, Tidlund J. Heat checking in hot work steels. Bull Cercle Etude Met 1979;14(5):185–93.

[13] Iwanaga S, Sakakibara Y, Konaga T, Nakamura M, Kamiya T. Initiation and propagation of heat checking in aluminum die casting dies. J Soc Mater Sci Japan 1987;36(405):604–9. https://doi.org/10.2472/jsms.36.604.

[14] Miquel B, Jean S, Le Roux S, Lamesle P, Rézaï-Aria F. Heat-checking of hot work tool steels. Eur Struct Integr Soc 2002;29:185–93. https://doi.org/10.1016/S1566-1369(02)80075-9.

[15] Ugues D, Rosso M, Albertinazzi M, Raimondi F, Silipigni A. The influence of plasma nitriding and post oxidising treatment on the resistance of AISI H11 to cycling immersion in molten aluminium alloy. Metall. Sci Technol 2004;22(1).

[16] Sjöström J, Bergström J. Thermal fatigue testing of chromium martensitic hot-work tool steel after different austenitizing treatments. J Mater Process Technol 2004; 153–154:1089–96. https://doi.org/10.1016/j.jmatprotec.2004.04.158.

[17] Le Roux S, Medjedoub F, Dour G, Rézaï-Aria F. Role of heat-flux density and mechanical loading on the microscopic heat-checking of high temperature tool steels under thermal fatigue experiments. Int J Fatigue 2013;51:15–25. https://doi.org/10.1016/j.ijfatigue.2013.02.004.

[18] Gorbach VG, Alekhin VG, Kurganova GL. Determining thermal fatigue of steels for die casting of aluminum alloys. Metal Sci Heat Treat 1977;19:982–5. https://doi.org/10.1007/BF00670172.

[19] Wang Y. A study of PVD coatings and die materials for extended die-casting die life. Surf Coat Technol 1997;94–95:60–3. https://doi.org/10.1016/S0257-8972(97)00476-3.

[20] Price JWH, Chang M, Kerezsi B. Cracking of carbon steel components due to repeated thermal shock. In: Structural Integrity and Fracture International Conference; 2004:305–14.

[21] Zhu Y, Schwam D, Wallace JF, Birceanu S. Evaluation of soldering, washout and thermal fatigue resistance of advanced metal materials for aluminum die-casting dies. Mater Sci Eng A 2004;379(1):420–31. https://doi.org/10.1016/j.msea.2004.03.020.

[22] Egorov VI, Plekhanov VA. Thermal fatigue of perlite steels under different oxidizing conditions. Strength Mater 1971;3:19–23. https://doi.org/10.1007/BF01530366.

[23] Persson A, Hogmark S, Bergström J. Failure modes in field-tested brass die casting dies. J Mater Process Technol 2004;148(1):108–18. https://doi.org/10.1016/j.jmatprotec.2004.01.052.

[24] Lamesle P, Salem M, Le Roux S, Dour G, Rezai-Aria F. Oxidation and corrosion effects on thermal fatigue behaviour of hot work tool steel X38CrMoV5 (AISI H11). Mater Sci Forum 2008;595–598:789–96. https://doi.org/10.4028/www.scientific.net/MSF.595-598.789.

[25] Pellizzari M, Ugues D, Cipolloni G. Influence of heat treatment and surface engineering on thermal fatigue behaviour of tool steel. Int Heat Treat Surf Eng 2013;7(4):180–4. https://doi.org/10.1179/1749514813Z.00000000091.

[26] Rousseau D, Riegert JP, Seraphin L, Tricot R. Fatigue thermique des aciers à outils pour travail à chaud. Revue de Métallurgie 1975;72(12):875–90. https://doi.org/10.1051/metal/197572120875.

[27] Peng W, Wu X, Min Y, Xu L. Comparison of thermal fatigue behavior of plasma nitriding with compound layer and without it of H13 steel. In: Proc. of 6th International Tooling Conference, Karlstad; 2002. p. 597–609.

[28] Pellizzari M, Molinari A, Straffelini G. Thermal fatigue resistance of gas and plasma nitrided 41CrAlMo7 steel. Mater Sci Eng A 2003;352(1–2):186–94. https://doi.org/10.1016/S0921-5093(02)00867-5.

[29] Srivastata A, Joshi V, Shivpuri R, Bhattacharya R, Dixit S. A multilayer coating architecture to reduce heat checking of die surfaces. Surf Coat Technol 2003; 163–164:631–6. https://doi.org/10.1016/S0257-8972(02)00690-4.

[30] Birol Y. Response to thermal cycling of plasma nitride hot work tool steel at elevated temperatures. Surf Coat Technol 2010;205(2):597–602. https://doi.org/10.1016/j.surfcoat.2010.07.035.

[31] Kundalkar D, Mavalankar M, Tewari A. Effect of gas nitriding on the thermal fatigue behavior of martensitic chromium hot-work tool steel. Mater Sci Eng A 2016;651:391–8. https://doi.org/10.1016/j.msea.2015.10.007.

[32] Manson SS. Thermal fatigue of Die Casting Dies–A Review and Proposed Future Program. Tech Rep. 01-72-05D. DCRF Technical Committee; 1972.

[33] Howes MAH. A study of thermal fatigue mechanisms. Symposium ASTM Committee E-9 on Thermal Fatigue of Materials and Components American Society for Testing and Materials, Philadelphia (USA), 1976; p. 86–105. Doi: 10.1520/STP27886S.

[34] Mitterer C, Holler F, Üstel F, Heim D. Application of hard coatings in aluminium die casting – soldering, erosion and thermal fatigue behaviour. Surf Coat Technol 2000;125(1–3):233–9. https://doi.org/10.1016/S0257-8972(99)00557-5.

[35] Spera DA. What is Thermal Fatigue? Symposium ASTM Committee E-9 on Thermal Fatigue of Materials and Components American Society for Testing and Materials, Philadelphia (USA), 1976; p. 3–9.

[36] Glenny E. The Influence of The Geometry on Thermal Fatigue Behavior. Thermal and Height Strain Fatigue, The Institute of The Iron and Steel Institute, 1967; p.346–63.

[37] Sabharwal KS. Thermal fatigue testing of die casting die steels. (1969). PhD Thesis. Paper 6967. https://scholarsmine.mst.edu/masters_theses/6967.

[38] Howes MAH. Evaluation of thermal fatigue resistance of metals using the fluidized bed technique. Fatigue at elevated temperatures ASTM Int 1973;520:242–54. https://doi.org/10.1520/STP38843S.

[39] Dobrzański LA, Mazurkiewicz J, Hajduczek E, Madejski J. Comparison of the thermal fatigue resistance and structure of the 47CrMoWVTiCeZr16-26-8 hot-work tool steel with X40CrMoV5-1 type one. J Mater Process Technol 2001;113(1–3): 527–38. https://doi.org/10.1016/S0924-0136(01)00721-X.

[40] Min Y, Xu L, Wu X. Influence of surface heat treatment on thermal fatigue behaviors of hot work steel. In: Proc. of 6th International Tooling Conference, Karlstad; 2002. p. 55–65.

[41] Schwam D, Wallace JF, Birceanu S. Effect of design factors on thermal fatigue cracking of die casting dies. DE-FC07-00ID138486, Case Western Reserve University/Dept of Materials Science and Engineering, Washington, DC (USA); 2004.

[42] Klobčar D, Tušek J, Taljat B. Thermal fatigue of materials for die-casting tooling. Mater Sci Eng A 2008;472(1–2):198–207. https://doi.org/10.1016/j.msea.2007.03.025.

[43] Birol Y. Thermal fatigue testing of Stellite 6-coated hot work tool steel. Mater Sci Eng A 2010;527(21–22):6091–7. https://doi.org/10.1016/j.msea.2010.06.015.

[44] Imran MK, Masood SH, Brandt M, Bhattacharya S, Gulizia S, Jahedi M, et al. Thermal fatigue behavior of direct metal deposited H13 tool steel coating on copper alloy substrate. Surf Coat Technol 2012;206(8–9):2572–80. https://doi.org/10.1016/j.surfcoat.2011.11.016.

[45] Mellouli D, Haddar N, Köster A, Ayedi HF. Hardness effect on thermal fatigue damage of hot-working tool steel. Eng Fail Anal 2014;45:85–95. https://doi.org/10.1016/j.engfailanal.2014.06.007.

[46] Terčelj M, Fazarinc M, Kugler G. Testing of thermal fatigue resistance of tools and rolls for hot working. Mater Geoenvironment 2017;64(3):161–8. https://doi.org/10.1515/rmzmag-2017-0010.

[47] Bombač D, Gintalas M, Kugler G, Terčelj M. Thermal fatigue behaviour of Fe-1.7 C-11.3 Cr-1.9 Ni-1.2 Mo roller steel in temperature range 500–700° C. Int J Fatigue 2019;121:98–111. https://doi.org/10.1016/j.ijfatigue.2018.12.007.

[48] Min Y, Bergström J, Wu X, Xu L. Oxidation and Thermal Fatigue Behaviors of Two Type Hot Work Steels During Thermal Cycling. J Iron Steel Res Int 2013;20:90–7. https://doi.org/10.1016/S1006-706X(13)60202-2.

[49] Malm S, Tidlund J. Increased life for die casting dies. In: Transactions of the 10th International Die Casting Congress, Paper No. IG-T79-051; 1979, p.1–14.

[50] Balandin YF. Thermal fatigue of metals. Metal Sci Heat Treat 1961;3(3):91–6. https://doi.org/10.1007/BF00810542.

[51] Salem M, Le Roux S, Dour G, Lamesle P, Choquet K, Rézaï-Aria F. Effect of aluminizing and oxidation on the thermal fatigue damage of hot work tool steels for high pressure die casting applications. Int J Fatigue 2019;119:126–38. https://doi.org/10.1016/j.ijfatigue.2018.09.018.

[52] Medjedoub F, Le Roux S, Dour G, Rézaï-Aria F. Effect of local stress on the heat-checking morphology in high temperature tool steels under thermal fatigue: transition from multi-axiality to uniaxiality. Mech Mater 2014;69(1):159–72. https://doi.org/10.1016/j.mechmat.2013.09.014.

[53] Qayyum F, Shah M, Shakeel O, Mukhtar F, Salem M, Rézaï-Aria F. Numerical simulation of thermal fatigue behavior in a cracked disc of AISI H-11 tool steel. Eng Fail Anal 2016;62:242–53. https://doi.org/10.1016/j.engfailanal.2016.01.015.

[54] Bruckel P, Lamesle P, Lours P, Pieraggi B. Isothermal oxidation behavior of a hot work tool steel. Mater Sci Forum 2004;461–164:831–8.

[55] Dour G, Salem M, Le Roux S, Texier D, Medjedoub F, Lamesle P, et al. AnT^2COK, an analytical model for cycling oxidation kinetics of hot-work toll steels in thermal cycling conditions. Corros Sci 2019;147:169–81. https://doi.org/10.1016/j.corsci.2018.11.009.

[56] Schütze M. Protective oxide scales and their breakdown. New York: John Wiley & Sons; 1997.

[57] Chen RY, Yeun WYD. Review of the high-temperature oxidation of iron and carbon steels in air or oxygen. Oxid Met 2003;59(5–6):433–68. https://doi.org/10.1023/A:1023685905159.

[58] Balaško T, Vončina M, Burja J, Šetina Batič B, Medved J. High-Temperature Oxidation Behaviour of AISI H11 Tool Steel. Metals 2021;11(5):758. https://doi.org/10.3390/met11050758.

[59] Min Y, Wu X, Wang R, Li L, Xu L. Prediction and Analysis on Oxidation of H13 Hot Work Tool Steel. J Iron Steel Res Int 2006;13:44–9. https://doi.org/10.1016/S1006-706X(06)60025-3.

[60] Christl W, Rahmel A, Schütze M. Behavior of oxide scales on 2.25Cr-1Mo steel during thermal cycling. I. Scales formed in oxygen and air. Oxid Met 1989;31:1–34. https://doi.org/10.1007/BF00665485.

[61] Tsujii N, Abe G, Fukaura K, Sunada H. Effect of testing atmosphere on low cycle fatigue of hot work tool steel at elevated temperature. ISIJ Int 1995;35(7):920–6. https://doi.org/10.1016/S0142-1123(97)82085-3.

[62] Oudin A, Lamesle P, Penazzi L, Le Roux S, Rézaï-Aria F. Thermo-mechanical fatigue behaviour and life assessment of hot work tool steels. Eur Struct Integr Soc 2002;29:195–201. https://doi.org/10.1016/S1566-1369(02)80076-0.

[63] Caliskanoglu D, Siller I, Ebner R, Leitner H, Jeglitsch F, Waldhauser W. Thermal fatigue and softening behavior of hot work tool steels. In: Proc of 6th International Tooling Conference, Karlstad; 2002. p. 707-19.

[64] Medvedeva A, Bergström J, Gunnarsson S, Andersson J. High-temperature properties and microstructural stability of hot-work tool steels. Mater Sci Eng A 2009;523(1–2):39–46. https://doi.org/10.1016/j.msea.2009.06.010.
[65] Markežič R, Mole N, Naglič I, Šturm R. Time and temperature dependent softening of H11 hot-work tool steel and definition of an anisothermal tempering kinetic model. Mater Today Commun 2020;22:100744. https://doi.org/10.1016/j.mtcomm.2019.100744.
[66] Mebarki N, Delagnes D, Lamesle P, Delmas F, Levaillant C. Relationship between microstructure and mechanical properties of a 5% Cr tempered martensitic tool steel. Mater Sci Eng A 2004;387–389:171–5. https://doi.org/10.1016/j.msea.2004.02.073.